# CFD-SIMULATION OF THREE-DIMENSIONAL DYNAMIC STALL ON A ROTOR WITH CYCLIC PITCH CONTROL

Johannes Letzgus, Manuel Keßler and Ewald Krämer

Institute of Aerodynamics and Gas Dynamics (IAG), University of Stuttgart
Pfaffenwaldring 21, Stuttgart, 70569, Germany
letzgus@iag.uni-stuttgart.de

**ABSTRACT**

Computational fluid dynamics (CFD) simulations of a two-bladed Mach-scaled rotor ($R = 0.65$ m, $Ma_{tip} = 0.6$, $Re_{tip} \approx 1 \times 10^6$) with 1/rev cyclic pitch control encountering three-dimensional dynamic stall are presented. The block-structured flow solver FLOWer is used along with the Menter SST turbulence model and a fifth-order spatial CRWENO scheme. A grid and time step dependency study shows the need of high resolution in space and time to properly resolve all stages of dynamic stall. The onset of flow separation in the outboard region of the rotor blade during its upstroke is found to be shock-induced. Flow pattern visualizations reveal the following evolution of a discrete $\Omega$-shaped vortex. Quickly thereafter a partially spanwise vortex occurs, which is bent towards the leading edge near the mid-span. An interaction with the blade tip vortex is noticed as a limitation of outboard-faced separation spreading. Only a small range of outboard radial sections could be found at which the flow pattern resembles two-dimensional dynamic stall. The superposition of an axial flow weakens the dynamic stall event and slightly changes the vortex pattern.

## 1. NOMENCLATURE

| | |
|---|---|
| $c$ | blade chord (m) |
| $C_l$ | sectional blade lift coefficient |
| $C_L$ | blade lift coefficient ($C_L = F_x/(\rho_\infty(\Omega R)^2\pi R^2)$) |
| $C_m$ | sectional blade pitching moment coefficient |
| $C_M$ | blade pitching moment coefficient ($C_M = M_z/(\rho_\infty(\Omega R)^2\pi R^3)$) |
| $C_p$ | pressure coefficient |
| $f$ | rotational frequency (Hz) |
| $k$ | reduced frequency ($k = \pi f c/u_\infty$) |
| $Ma$ | Mach number |
| $p$ | pressure (Pa) |
| $r$ | nondimensional radial distance |
| $R$ | rotor blade radius (m) |
| $Re$ | Reynolds number |
| $rev$ | rotor revolution |
| $s$ | cell size (m) |
| $t$ | maximum airfoil thickness (m) |
| $u_\infty$ | free stream velocity (m/s) |
| $x$, $y$, $z$ | normal, streamwise and spanwise direction (blade root system, m) |
| $y^+$ | dimensionless wall distance |
| $\theta$ | geometric angle of attack (deg) |
| $\rho$ | density (kg/m$^3$) |
| $\psi$ | azimuth angle (deg) |
| $\Omega$ | rotational frequency (rad/s) |
| $\uparrow$ | on the upstroke |
| $\downarrow$ | on the downstroke |

Subscripts

| | |
|---|---|
| $75$ | at the radial station $r/R = 0.75$ |
| $C1$, $2$, $3$ | case one, two, three |
| $m$ | mean value |
| $s.s.$ | static stall |
| $tip$ | at the blade tip |
| $\infty$ | at the far field |

## 2. INTRODUCTION

Dynamic stall describes a complex, unsteady flow phenomenon, which occurs on helicopter rotor blades in high-speed forward or maneuvering flight. Due to low flow velocities and high blade pitch angles on the retreating side of the blade, high effective angles of attack are reached and flow separation sets in. During the phase of dynamic stall the blade lift and nose-down pitching moment increase rapidly, exceeding by far their static maximum values[1]. However, since those highly unsteady airloads significantly limit the overall flight performance of a helicopter[2] it is of great interest to fully understand the formation and evolution of dynamic stall vortices. The investigation

of this phenomenon is still one of the most challenging topics of experimental research and computational fluid dynamics.

Recent work of Klein et al.[3] compared two- and three-dimensional CFD-computations of airfoils in dynamic stall with experimental wind tunnel results. Gardner and Richter[4] numerically investigated the influence of rotation, while Spentzos et al.[5] and Kaufmann et al.[6] did numerical research into three-dimensional dynamic stall on a pitching finite wing. Further three-dimensional effects on a pitching airfoil were shown by Nilifard et al.[7].

In the framework of a research project of the Deutsche Forschungsgemeinschaft (DFG) between the German Aerospace Center (DLR) and the Institute of Aerodynamics and Gas Dynamics (IAG) of the University of Stuttgart, the DLR currently builds a Mach-scaled rotor test facility[8] to investigate the three-dimensional dynamic stall phenomenon. Here a cyclic blade pitch angle variation can be controlled via a conventional swashplate. Supporting this experiment, CFD-simulations of a rotor with sinusoidally pitching blades are conducted at the IAG. The main goal of the present high-resolution numerical investigation is to capture the phenomenon on a two-bladed rotor with cyclic pitch control and to gain insight into the three-dimensional vortical structures and flow patterns occurring during dynamic stall.

Three test cases are presented, as listed in Tab. 1: A rotor operating in a hover-like state in still air with a 1/rev cyclic pitch control resulting in a $\theta_{75} = 9.2° - 10° \sin(\psi)$ pitching motion. In the second case the mean geometric pitch angle is increased to $\theta_m = 17.2°$, while the amplitude $\hat{\theta}$ is kept at $10°$. Thirdly the blade motion of the second case is used again but an axial flow with a free stream velocity of $u_\infty = 14\ \mathrm{m/s}$ is superimposed, creating a climb flight-like environment. Therefore the third case reproduces the wind tunnel experiments conducted at DLR.

**Tab. 1.** Overview of the three cases investigated. The pitching motion of the blade is $\theta_{75}(\psi) = \theta_m - \hat{\theta}\sin(\psi)$.

| case | $\hat{\theta}$ [°] | $\theta_m$ [°] | $u_\infty$ [m/s] |
|---|---|---|---|
| 1 | 10.0 | 9.2 | 0.0 |
| 2 | 10.0 | 17.2 | 0.0 |
| 3 | 10.0 | 17.2 | 14.0 |

## 3. COMPUTATIONAL SETUP

The block-structured finite-volume Reynolds Averaged Navier Stokes (RANS) solver FLOWer[9] of the DLR is used for the present computations. While the flow is fully turbulent, the Menter SST turbulence model[10] is used due to its known capability of capturing separation effects[3,11]. Acceptable computation times are achieved with an implicit dual time stepping method of second order for time integration and a three-level multigrid method. For long-time conservation of vortical structures, the fifth-order spatial Compact-Reconstruction Weighted Essentially Non-Oscillatory (CRWENO) scheme[12] is applied for the final computations in the background grid and in the blade grids. The noticeable reduction of numerical dissipation when using the CRWENO flux reconstruction and its validation regarding rotor simulations with the FLOWer code was shown recently[13,14].

The geometries of the components of this numerical investigation are based on the Rotor Test Facility of the DLR in Göttingen[8]. There the rotor is mounted on a test bench which is integrated into an Eiffel-type wind tunnel. The wind tunnel has a rectangular nozzle with the size of $1.6\ \mathrm{m} \times 1.6\ \mathrm{m}$ and provides a maximum free stream velocity of $u_\infty = 14\ \mathrm{m/s}$. Fig. 1 shows the CAD model of the rotor test bench positioned in front of the wind tunnel nozzle. The rotor radius is $R = 0.65\ \mathrm{m}$ with a mean chord length of $c_{mean} = 72\ \mathrm{mm}$ and a thickness of $t = 6.5\ \mathrm{mm}$. It uses a DSA-9A airfoil shape with a parabolically shaped SPP8 blade tip without anhedral. The chord length at the blade tip is $c_{tip} = 24\ \mathrm{mm}$. From the blade's root to its tip a linear negative twist with $\Delta\theta = -9.3°$ is applied. The rotation axis of the pitching motion is coaxial to the quarter-chord line of the blade. The rotor is operated at a rotational frequency of $f_{rot} = 50\ \mathrm{Hz}$ (reduced frequency at $r/R = 0.75$ is $k_{75} = 0.074$), leading to a Mach number of $Ma_{tip} = 0.6$ and a Reynolds number of approximately $Re_{tip} = 1 \times 10^6$.

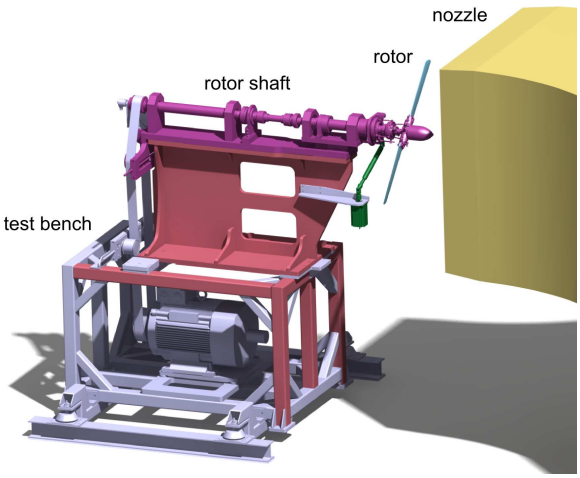



**Fig. 1.** CAD model of the actual rotor test bench in front of the wind tunnel nozzle.

For the present simulations a baseline and a fine rotor blade grid were used. In general the block-structured rotor blade grid is of the C-H type. Detail a) of Fig. 2 shows a slice through the grid of the fine setup at a radial station near the blade tip. In order to resolve all stages of three-dimensional dynamic stall – that is, flow separation and forming of vortical structures at the leading edge, its downstream convection and shedding into the wake and the reattachment of flow – a high spatial resolution is needed at every part of the rotor blade, as it can be seen in Detail b) of Fig. 2. Streamwise, normal and spanwise spatial resolutions of both blade grids are compared in Tab. 2. In both cases, the height of the first cell off the wall is approximately $\Delta s = 1 \times 10^{-6}\ \mathrm{m}$, leading to a dimensionless wall distance of $y^+ < 1$ on the whole blade surface.

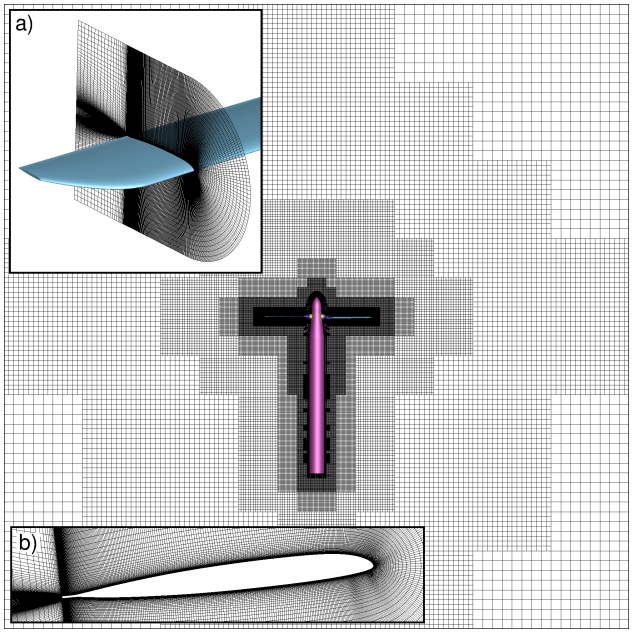



**Fig. 2.** Rotor grid embedded into the fine Cartesian background grid. **Detail a)** Slice through the C-H-type blade grid. **Detail b)** Fine grid near the blade surface and airfoil shape.

To take the actual rotor hub geometry into account a simplified shape of the blade mount was generated and then meshed with a block-structured O-grid. Since the blade mount encounters the same pitching motion as the rotor blade, a connector grid is used to provide a good overlap with the spinner grid. Fig. 3 shows the surface grids and Chimera interpolation regions of these components. The rotor shaft and its bearing are represented in this CFD-simulation by a cylinder, which is connected to the spinner and extended to the far wake. In contrast to the rotor blade and hub grid, no grid refinement of the spinner grid towards the surface and an inviscid wall boundary condition is applied. The error resulting from the neglected boundary layer (BL) effects of the spinner wall is expected to be minor since flow velocities are low near the rotation axis of the rotor. Furthermore the distance between the spinner wall and dynamic stall relevant regions on the rotor blade seems large enough to justify this simplification.

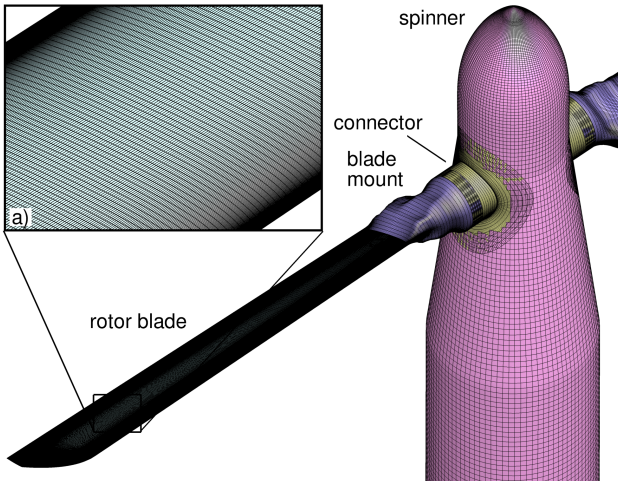



**Fig. 3.** Surface grids of the rotor components showing the Chimera interpolation regions. **Detail a)** Grid on the blade surface at $r/R \approx 0.8$.

**Tab. 2.** Grid resolution of the computational setup.

| **rotor blade grid** | | |
|---|---|---|
| streamwise & normal | baseline | fine |
| $s/c_{local}$ at leading edge | 0.075 % | 0.045 % |
| $s/c_{local}$ at trailing edge | 0.075 % | 0.045 % |
| $s/c_{local}$ maximum | 1.0 % | 0.8 % |
| points around airfoil | 433 | 593 |
| points in BL | 37 | 41 |
| spanwise | baseline | fine |
| $s/c_{mean}$ at root | 6 % | 6 % |
| $s/c_{mean}$ at r/R = 0.7 | 2.8 % | 2.2 % |
| $s/c_{mean}$ at blade tip | 0.9 % | 0.9 % |
| **background grid** | | |
| | baseline | fine |
| $s_{min}/c_{mean}$ at rotor disc | 10 % | 5 % |
| $s_{max}/c_{mean}$ at farfield | 160 % | 160 % |

The Chimera technique is not only used to connect the grids of the components shown in Fig. 3, but also to embed them into the Cartesian background grid, see Fig. 2. Matching the two versions of rotor blade grids, a baseline and fine background grid are used, as listed in Tab. 2. The background grid was auto-generated and uses the “hanging nodes” technique to coarsen the grid with increasing distance from the rotor disc. Both background grids extent to a distance of $5.7\ \mathrm{R}$ from the rotor origin in all three space dimensions and use a far field boundary condition. While the finest grid spacing of the baseline background grid near the rotor disc is $s/c_{mean} = 10\ \%$ respectively $s/c_{mean} = 5\ \%$ with the fine version, the spacing

near the grids of blade mount, connector and spinner is kept at $s/c_{mean} = 10\ \%$.

The overall block and cell numbers of each component of the present simulation are listed in Tab. 3. Regarding the temporal discretization of the rotor blade motions, time steps between 720 ($\Delta\psi = 0.5°$) and 2000 time steps per period ($\Delta\psi = 0.18°$) were investigated. All simulations were carried out on the CRAY XC40 (Hornet) computer cluster of the High Performance Computing Center Stuttgart (HLRS) using 1560 cores (baseline setup) and 2832 cores (fine setup), respectively.

**Tab. 3.** Block and cell numbers of grid components.

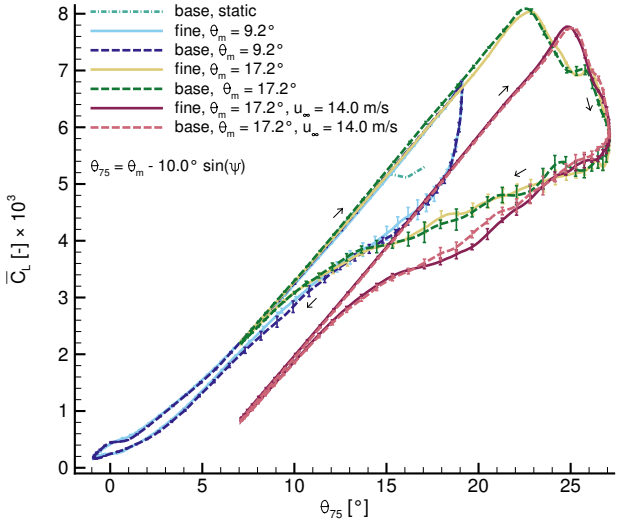
| component | grid | block no. | cell no. (million) |
|---|---|---|---|
| rotor blade | baseline | $2 \times 564$ | $2 \times 8.45$ |
| | fine | $2 \times 863$ | $2 \times 16.80$ |
| background | baseline | 532 | 4.52 |
| | fine | 1393 | 14.79 |
| blade mount | both | $2 \times 18$ | $2 \times 0.20$ |
| connector | both | $2 \times 6$ | $2 \times 0.08$ |
| spinner | both | 38 | 0.41 |
| **total** | **baseline** | **1746** | **22.39** |
| | **fine** | **3205** | **49.36** |

## 4. RESULTS AND DISCUSSION

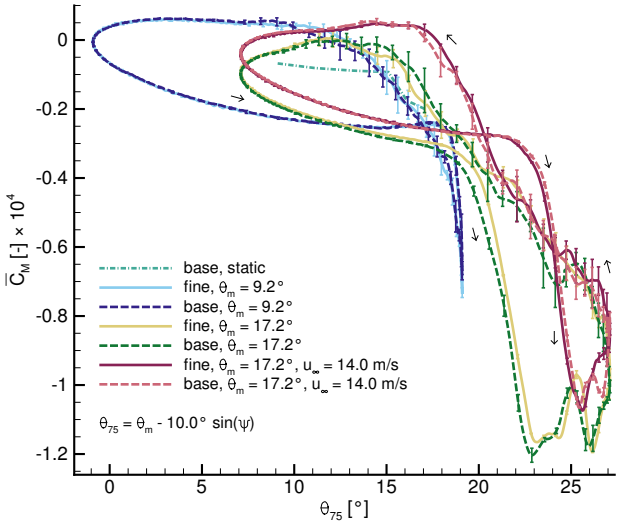
### 4.1. Load characteristics of 3D dynamic stall

In this numerical investigation the described rotor was simulated with a cyclic pitch variation in order to trigger dynamic stall. Fig. 4 shows the integral loads on a rotor blade during a complete cycle for the three cases investigated. For comparison, the polar curve of the static case is plotted, too. Here the time step is $\Delta\psi = 0.25°$ (1440 steps per cycle). The loads are averaged over four dynamic stall cycles (two rotor revolutions), the error bars represent the standard deviation.

The main characteristics of dynamic stall regarding the loads are present at all three unsteady cases: With increasing angle of attack the blade lift (Fig. 4(a)) almost linearly increases well beyond its static maximum, which is at about $\theta_{75_{s.s.}} = 15.1°$. Eventually the lift breaks down rapidly and a strong hysteresis becomes apparent. While the lift is overshooting, a sudden and steep drop in nose-down pitching moment sets in (Fig. 4(b)). Increasing the mean angle of attack leads to higher maximum loads and stronger hysteresis, which is known from two-dimensional dynamic stall[2]. Exclusively in the second case and around $\theta_{75_{C2}} = 25.5°$ – while the blade is still on its




(a) rotor blade lift coefficient $C_L$




(b) rotor blade pitching moment coefficient $C_M$

**Fig. 4.** Integral loads of the rotor blade during dynamic stall using two different grids. The loads are averaged over four dynamic stall cycles, time step $\Delta\psi = 0.25°$.

upstroke but has already stalled – a noticeable peak in integral lift and pitching moment indicates a second dynamic stall event. In case three an axial flow is superimposed, which results in an overall lift reduction since the effective angles of attack are reduced. Comparing case two and three (same pitching motion), the characteristic events of dynamic stall are therefore shifted to higher angles of attack. The maximum of lift and negative pitching moment as well as the amount of hysteresis are slightly lower in case three.

The variation of the standard deviation during the dynamic stall cycles of all three cases is in good agreement with experimental results[3,6,7], since on

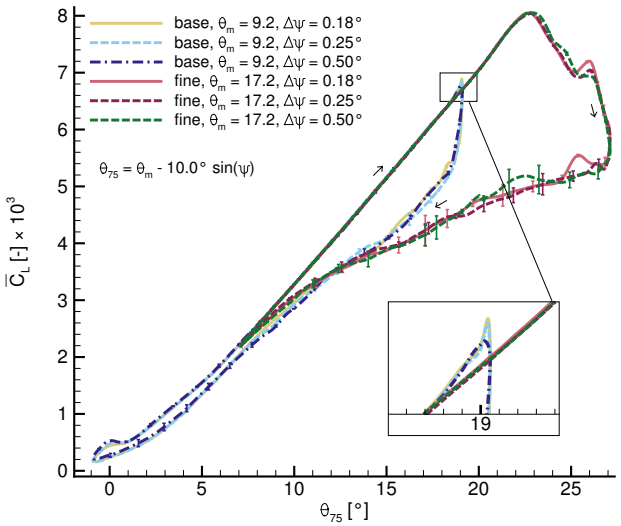
the downstroke of the rotor blade, the flow on the upper side of the blade is fully separated and of rather chaotic nature.

### 4.2. Grid and time step dependency

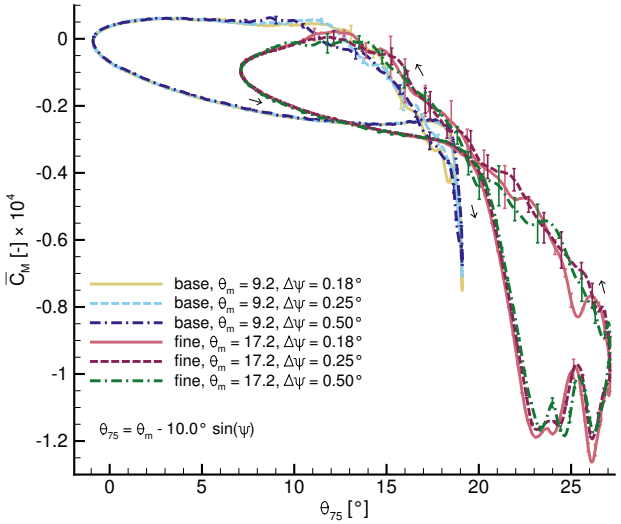
During three-dimensional dynamic stall one encounters all kinds of complex flow phenomena like strong blade tip vortices, unsteady, three-dimensional flow separation with vortex shedding and flow reattachment as well as supersonic flow with compression shocks. Since this is still a very demanding task for computational fluid dynamics, a grid and time step dependency study was carried out to gain confidence in the numerical setup.

In case one, which exhibits the weakest regime of dynamic stall, the integral lift during the complete cycle as well as the point of lift and moment stall is basically the same comparing the two grids. However, the nose-down pitching moment of the fine grid drops about $7\ \%$ deeper than on the baseline grid. In case two, which can be considered as deep dynamic stall by the definition of McCroskey[1], the fine grid produces a slightly lower lift in the linear and peak regime of the polar curve. Lift and moment stall occur about $0.5°$ earlier on the baseline grid. Corresponding to the $0.6\ \%$ higher maximum lift of the baseline solution, a lower minimum pitching moment is reached there, too. Regarding the second dynamic stall event in case two, the peak is more distinct and occurs slightly later on the fine grid, but the baseline grid captures this stall phenomenon as well. In case three, generally good agreement between the calculated loads of the two grids is found. The baseline grid solution exhibits the lift stall slightly later and – judging by the small peak in the pitching moment around $\theta_{75_{C3}} = 26.5°$ – involves a weak secondary dynamic stall event. In general the differences between the baseline and fine grid are small regarding the calculated integral loads. Although the numerical solution is not completely grid-converged, the baseline grid captures key characteristics of three-dimensional dynamic stall. Nevertheless, following results of this work are based on the fine grid solution.

Since dynamic stall is known as a highly unsteady flow phenomenon, a fine time discretization is appropriate. Recent investigations by Nilifard et al.[7] and Kaufmann et al.[6] showed good results using 720 time steps for an oscillating airfoil and 1500 – 3000 time steps for an oscillating finite wing, respectively. Here three time steps were investigated: $\Delta\psi = 0.18°$ (2000 steps/ cycle), $\Delta\psi = 0.25°$ (1440 steps/ cycle) and $\Delta\psi = 0.50°$ (720 steps/ cycle). Fig. 5 shows the integral loads of a rotor blade during a complete dynamic stall cycle using different time steps for case one with the baseline grid and for case two with the fine grid. The loads are averaged over two dynamic stall cycles (one rotor revolution), the error bars represent the standard deviation again.




(a) rotor blade lift coefficient $C_L$




(b) rotor blade pitching moment coefficient $C_M$

**Fig. 5.** Integral loads of the rotor blade during dynamic stall using different time steps. The loads are averaged over two dynamic stall cycles.

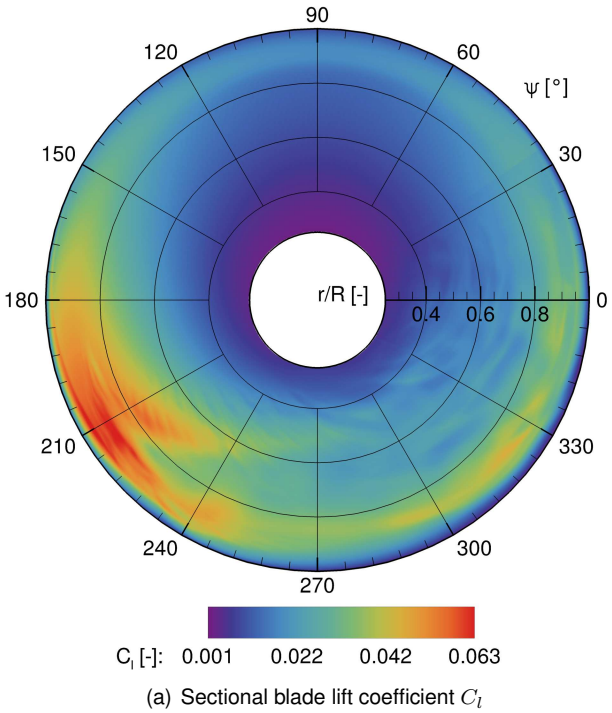
In case one, the coarsest time step solution does not show that sharp of a lift peak and underestimates the negative pitching moment during moment stall by $10\ \%$ compared to the finest time step. Similarly to the grid dependency study, it seems nearly impossible to achieve complete convergence of the minimum pitching moment of case one with reasonable computational effort. Besides the small peak region, time convergence of integral loads is reached

throughout the upstroke and most parts of the downstroke of case one. In case two with the fine grid, the coarsest time step solution shows a slightly delayed lift stall and lacks the distinct second peak in lift around $\theta_{75_{C2}} = 25.5°$. Since the pitching moment curve exhibits this peak, although with lower extreme values, the secondary dynamic stall events seem to lose strength with the coarsening of the time step. This applies to the overall differences between the $\Delta\psi = 0.25°$ and $\Delta\psi = 0.18°$ solution as well. At the beginning of the downstroke, only the finest time step shows a low third load peak. However, main load characteristics of primary lift and moment stall of case two are captured qualitatively well with all investigated time steps. Following results are based on the $\Delta\psi = 0.25°$ time step, as this step size was accepted as a good trade-off between time convergence and computational effort.

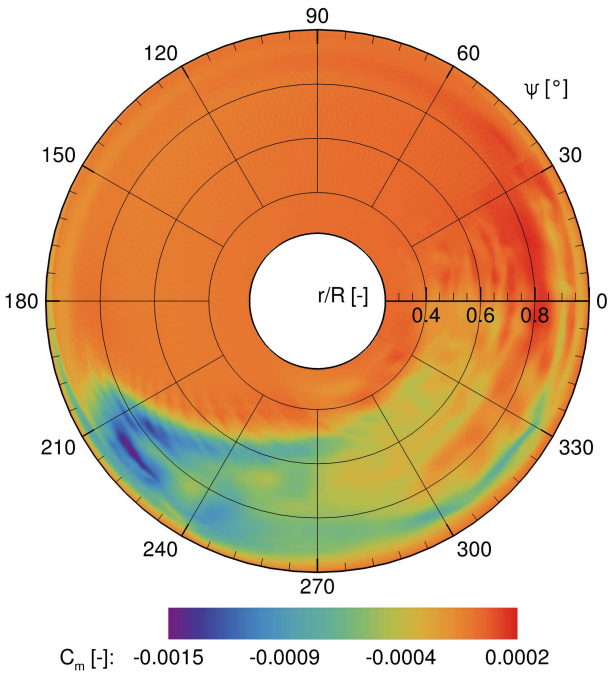
### 4.3. Three-dimensional aspects of dynamic stall

To establish a better understanding of the three-dimensionality of dynamic stall on a rotor with cyclic pitch control, the radial and azimuthal load distribution of a rotor blade during deep dynamic stall is shown in Fig. 6. The data shown is based on one revolution of case two with a pitching motion of $\theta_{75} = 17.2° - 10° \sin(\psi)$. Therefore the minimum geometric angle of attack is at $\psi = 90°$, the maximum at $\psi = 270°$, the rotation is counter-clockwise. The lift distribution in Fig. 6(a) shows basic characteristics of a rotor with cyclic pitch control: In quadrant one and two, geometric angles of attack are lower than in quadrant three and four, consequently most lift is generated in the second half. Since the Mach number varies along the rotor blade span, there is only low lift generation in the inboard region of the rotor. Reaching the blade tip the lift drops to zero due to three-dimensional flow. In the first half of the third quadrant there is a fine strip of high lift near the blade tip. Here the blade tip vortex originates radially further inboard and induces high local flow velocities leading to regions of low pressure on the suction side of the blade. Since the strength of the tip vortex correlates with the lift of the rotor blade, its influence varies during one revolution.

Regarding the occurrence of dynamic stall, there is a region of particularly high lift in the first half of the third quadrant and the span station of $r/R \approx 0.9$ with a maximum around $\psi = 215°$, which corresponds to the maximum integral lift represented by the ochre curve in Fig. 4(a). Starting from $\psi \approx 180°$ the region of high lift expands towards the mid-span of the blade. With an increasing azimuth angle, the integral lift stall is noticeable as a sudden loss of lift around $r/R = 0.82$. A broader strip of high lift from $r/R \approx 0.85$ to $r/R \approx 0.95$ remains until $\psi \approx 232°$. The second dynamic stall event can be seen at $\psi \approx 240°$ at the outboard section of the blade, where lift increases again for only some degrees of azimuth. Fig. 6(b) shows the characteristic peak in negative pitching moment dur-




(a) Sectional blade lift coefficient $C_l$




(b) Sectional blade pitching moment coefficient $C_m$

**Fig. 6.** Radial and azimuthal load distribution of a rotor blade during one cycle of deep dynamic stall. The pitching motion is $\theta_{75} = 17.2° - 10° \sin(\psi)$ (case two).

ing dynamic stall. The known correlation between lift and pitching moment during dynamic stall is apparent as well.

On the downstroke of the blade the load distribution is disturbed and short strips of high lift and low pitching moment suggest the occurrence of several minor dynamic stall vortices. The matching surface streamlines in Fig. 9 indicate the high degree of flow separation and three-dimensional flow during this stage, which leads to this long-lasting region of unsteady load distribution. At $r/R \approx 0.9$ throughout the fourth quadrant relatively high loads are generated. Fig. 7 shows instantaneous isosurfaces of the $\lambda_2$-criterion and streamlines at the outboard section of the blade at $\psi = 297°$. It exhibits the presence of several streamwise vortical structures with one stronger vortex originating near the leading edge at $r/R \approx 0.85$. This vortex resembles the conventional tip vortex, induces low pressure underneath and locally generates high lift. Since the low pressure region even extends to the trailing edge, the nose-down pitching moment is high as well. The streamwise vortical structures could represent the roll up of the free shear layer during dynamic stall, as supposed by DiOttavio[15].

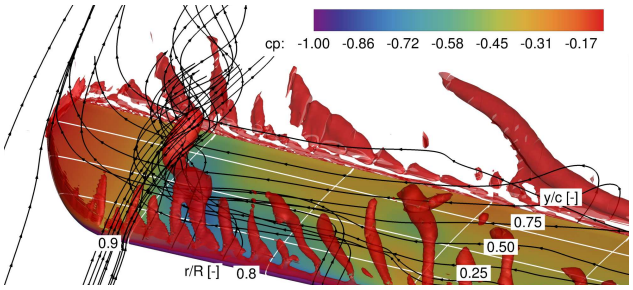



**Fig. 7.** Instantaneous isosurfaces of the $\lambda_2$-criterion and streamlines indicate streamwise vortical structures creating low surface pressure during downstroke, $\psi = 297°$, $\theta_{75} = 26.0° \downarrow$.

Further insight into three-dimensional aspects of dynamic stall is provided with Fig. 9, which shows the instantaneous distribution of the surface pressure coefficient $C_p$ and surface streamlines on the suction side of a rotor blade at certain stages of dynamic stall in case two. The surface streamlines are based on the velocities of the grid points of the first cells around the surface. At the azimuth of $\psi \approx 176°$ (Fig. 9(a)) the blade is already pitched $1.3°$ beyond its static stall angle, but the flow remains attached over most parts of the blade. Near the trailing edge of the inboard section, where geometric angles of attack are high and streamwise flow velocities are low, streamlines begin to bend outboard. This indicates a radial flow towards the blade tip and therefore the onset of trailing edge separation. As the azimuth angle increases, the radial flow grows and full separation occurs over most parts of the trailing edge (e.g. Fig. 9(c)).

However, the onset of dynamic stall can be seen in Fig. 9(a) near the leading edge around the radial station of $r/R \approx 0.85$. Here, directly downstream of the suction peak, the spanwise surface streamlines indicate partial separation. Mach number contours at this azimuth angle, as shown in Fig. 8, reveal supersonic flow and a normal shock. Shock-induced separation leading to dynamic stall was experimentally observed at oscillating airfoils at comparable Mach numbers before[16]. Although the present region of supersonic flow is small, this flow separation is assumed to be shock-induced, too.

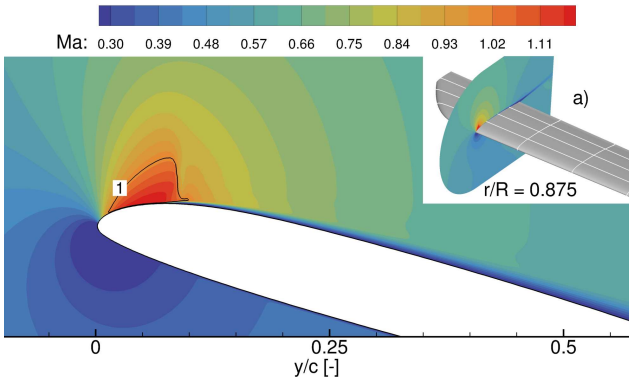



**Fig. 8.** Mach number contours at $r/R = 0.875$ at the onset of dynamic stall indicating supersonic flow and a normal shock. Case two at $\psi = 175.8°$, $\theta_{75} = 16.4° \uparrow$ (compare Fig. 9(a)).

With increasing azimuth the flow in this region of the blade does not recover; on the contrary, the flow separation spreads quickly, as Fig. 9(b) shows. This development is not limited to the deep dynamic stall of case two but occurs equally in the other cases. The spreading of the flow separation can be seen in Figs. 9(b) - 9(e): The separation line moves downstream and towards the blade mid-span, while the radial flow component is negligible, except for the stalled tailing edge. In the region upstream of the separation line the flow is reversed and surface pressure is low, generating a noticeable amount of lift, as already seen in Fig. 6(a). Until $\psi \approx 203°$ (Fig. 9(d)) there is a narrow region next to the blade tip around $r/R = 0.95$ and downstream of the quarter-chord line where flow stays attached and almost undisturbed. Here the influence of the blade tip vortex seems to weaken the outboard-faced effects of dynamic stall. This is in good agreement with an experimental investigation of an oscillating finite wing by Wolf et al.[17], using the identical airfoil and blade tip geometry.

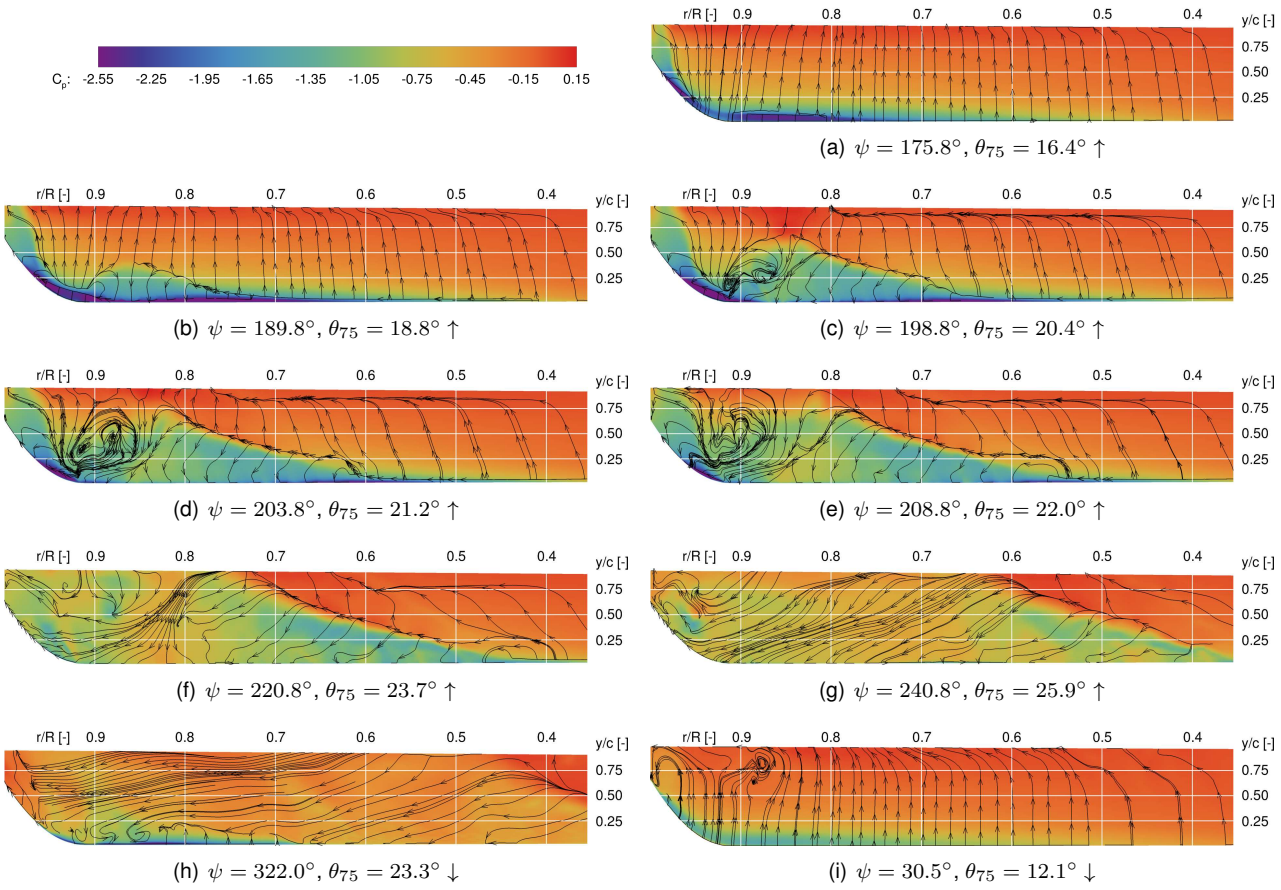
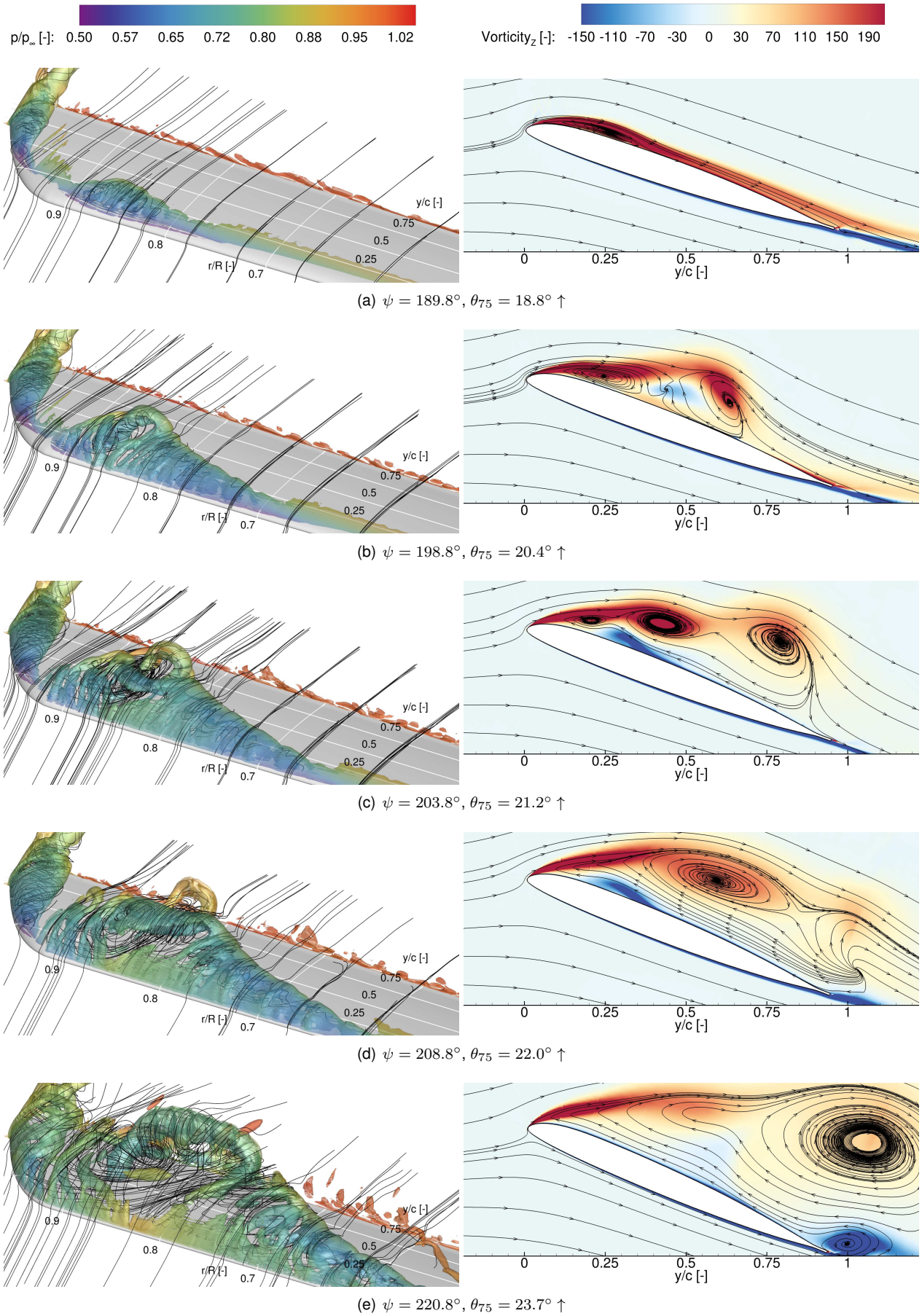



**Fig. 9.** Instantaneous distribution of the pressure coefficient $C_p$ and upper surface streamlines during deep dynamic stall on a pitching rotor blade with $\theta_{75} = 17.2° - 10° \sin(\psi)$ (case two).

Around $r/R = 0.9$ the circular surface streamlines indicate the presence of vortical structures normal to the blade surface. For a long period of time the flow pattern and low pressure distribution in this region is relatively stable and is therefore the reason for the broad strip of high lift discussed before. After integral lift stall ($\psi \approx 215°$) the circular flow near the surface at the outboard section seems to disappear, the pressure rises and radial flow begins to dominate. At $\psi \approx 322°$ during the downstroke, the flow reattaches at the leading edge of the outboard section. However, not until $\psi \approx 30°$ reattachment takes place over most parts of the rotor blade.

The three-dimensional vortical structures occurring during dynamic stall are visualized on the left of Fig. 10 by means of instantaneous isosurfaces of the $\lambda_2$-criterion and volume streamlines. On the right vorticity contours and in-plane streamlines at the radial station of $r/R = 0.84$ are shown. In Fig 10(a) the blade has already exceeded its static stall angle by $3.7°$. Circular streamlines indicate the formation of a vortex near the leading edge between $r/R = 0.8$ and $r/R = 0.9$. At this point the vortex is attached to the surface and its vertical extent is small. The discrete blade tip vortex can be seen, too. Ten degrees of azimuth later (Fig 10(b)), the vortex has grown in size, detached from the surface and evolved into the characteristic $\Omega$-shape, which is well known from pitching finite wings[6,5]. Since the vortex has convected downstream the quarter chord line, extra lift generation shifts towards the trailing edge and the nose-down pitching moment rapidly increases. The in-plane streamlines already indicate the formation of a second vortex at the leading edge. This must not be confused with the second dynamic stall event leading to the second peak in integral loads, which does not occur until $\psi \approx 240°$. Then Fig. 10(c) to Fig. 10(e) illustrate the evolution of the vortical structures during the upstroke of the rotor blade: The primary, $\Omega$-shaped vortex convects further downstream and away from the surface, but does not significantly grow in size. The second vortex seems to end normal to the blade's surface at $r/R \approx 0.9$ and to merge with the outboard leg of the $\Omega$-vortex, creating the circular flow pattern near the surface as observed in Fig. 9. Between $r/R \approx 0.9$ and $r/R \approx 0.8$ the second vortex forms a lifted, almost spanwise filament and then




(a) $\psi = 189.8°$, $\theta_{75} = 18.8°$ ↑

(b) $\psi = 198.8°$, $\theta_{75} = 20.4°$ ↑

(c) $\psi = 203.8°$, $\theta_{75} = 21.2°$ ↑

(d) $\psi = 208.8°$, $\theta_{75} = 22.0°$ ↑

(e) $\psi = 220.8°$, $\theta_{75} = 23.7°$ ↑

**Fig. 10.** Visualization of dynamic stall on a pitching rotor blade with $\theta_{75} = 17.2° - 10° \sin(\psi)$ (case two). Left: Instantaneous isosurfaces of the $\lambda_2$-criterion colored with $p/p_\infty$ and streamlines indicate vortical structures on the upper side of the blade. Right: Instantaneous vorticity contours and in-plane streamlines at $r/R = 0.84$.

bends towards the leading edge and back to the surface, ending almost at mid-span of the blade. This asymmetric and skewed arch-shape of the second vortex seems to be a result of the interaction with the blade tip vortex, which limits the outboard spreading, and the varying Mach number along the span. The tip vortex itself grows in size as the blade approaches maximum lift. Furthermore in-plane streamlines in Fig. 10(c) indicate the formation of a third vortex near the leading edge, which vanishes or merges with the second vortex soon, as it has already disappeared $\Delta\psi = 5°$ later (Fig. 10(d)). After the second vortex has reached the trailing edge and integral lift breaks (Fig. 10(e)), the flow on the upper side of the rotor blade is highly three-dimensional and even the tip vortex becomes disturbed and less compact. This evolution of the tip vortex is similar to the experimental results of Wolf et al.[17] on an oscillating finite wing. Interestingly, around the radial station of $r/R = 0.85$ – where load and surface pressure distribution revealed to be a crucial contribution to the point of integral lift and moment stall – the flow is quite comparable to the one of two-dimensional dynamic stall.

Between the azimuth of $\psi \approx 235°$ and $\psi \approx 245°$ the secondary dynamic stall event, which generates a second but smaller peak in lift and pitching moment, takes place, as a spanwise vortex forms at the leading edge of the outboard region. It then convects downstream, grows in size and is shed into the wake. Fig. 11 shows the flow at $\psi = 240.8°$, when this vortex has passed the mid-chord line. The ongoing collapse of the blade tip vortex is visible, too.

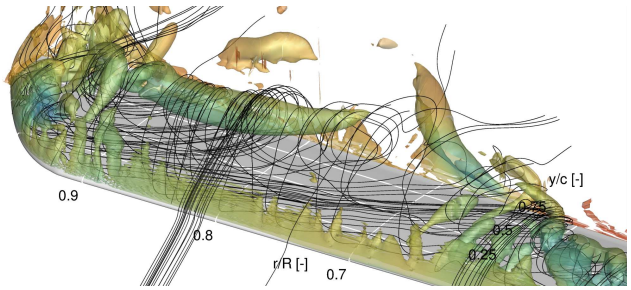



**Fig. 11.** Instantaneous isosurfaces of the $\lambda_2$-criterion colored with $p/p_\infty$ and streamlines visualize the secondary dynamic stall vortex in case two, $\psi = 240.8°$, $\theta_{75} = 25.9° \uparrow$.

In case one, which is considered as the weakest dynamic stall event investigated, the evolution of the vortical structures of primary dynamic stall and the overall flow topology is qualitatively the same as in case two. A snapshot of the flow field of case one can be seen in Fig. 12. At this point the blade encounters moment stall and is at an equal stage as the blade in case two in Fig. 10(c). Both the $\Omega$-shaped first vortex and the sectionally almost spanwise second one occur, however, the spanwise spreading is lower in case one.

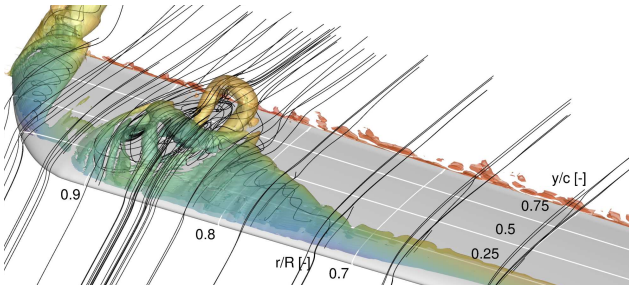
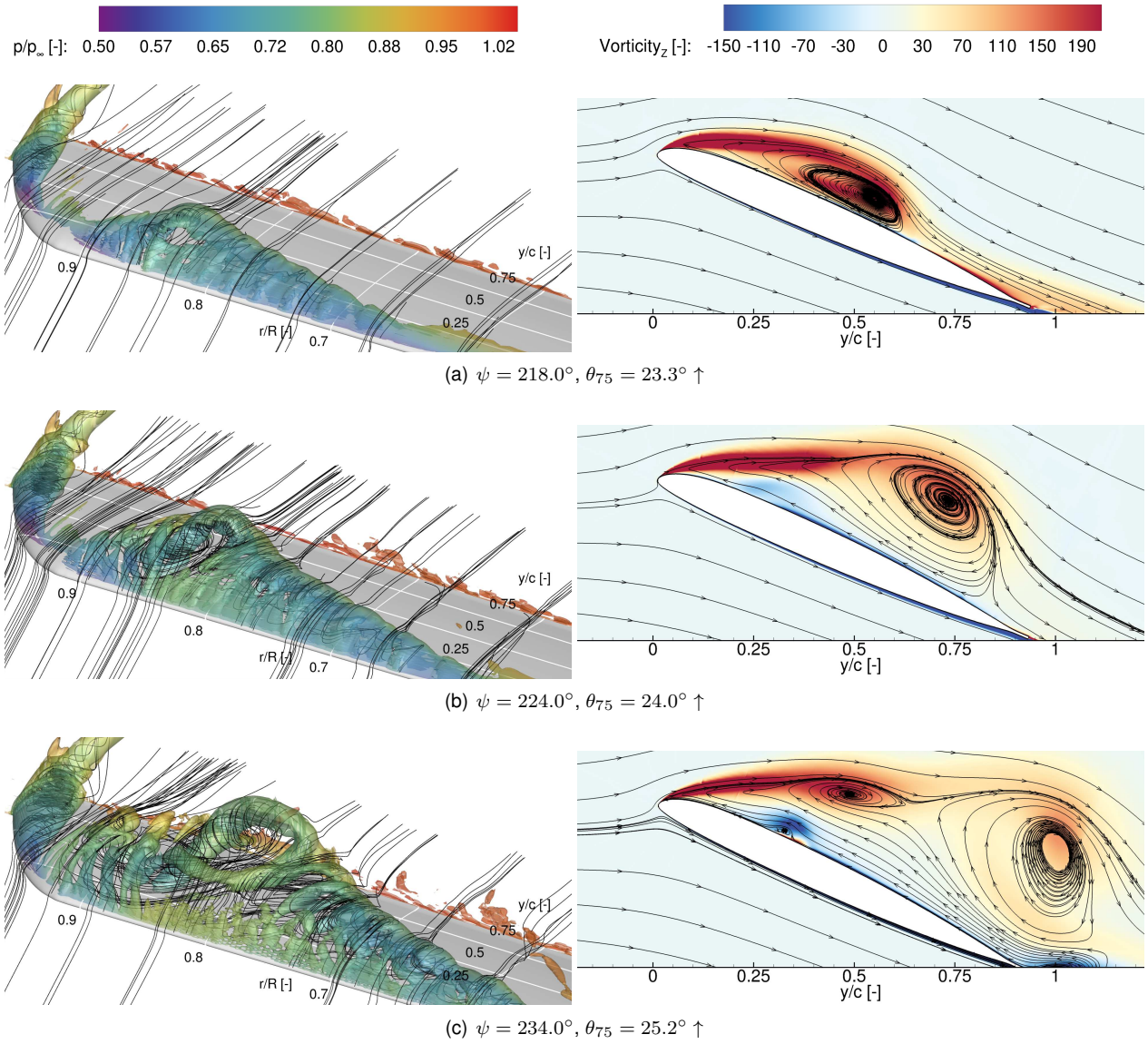



**Fig. 12.** Instantaneous isosurfaces of the $\lambda_2$-criterion colored with $p/p_\infty$ and streamlines visualize primary dynamic stall in case one, $\psi = 257.0°$, $\theta_{75} = 18.9° \uparrow$.

Regarding case three, which uses the same pitching motion as case two but with a superimposed axial flow with a free stream velocity of $u_\infty = 14\ \mathrm{m/s}$ – creating a climb flight- or wind tunnel-like environment – the vortex development somewhat differs from both other cases. In Fig. 13, showing case three during dynamic stall, the same visualization methods are used as in Fig. 10. Both the $\lambda_2$-isosurfaces and the in-plane flow pattern of the first two snapshots indicate the presence of only one vortex. At this stage of dynamic stall, before maximum integral lift is reached, the cases without a superimposed axial flow already showed a discrete $\Omega$-vortex and a second, partially spanwise vortex. Here the single vortical structure seems to have the features of the two vortices combined: A less distinct $\Omega$-shape is formed with its outboard leg ending normal to the surface, creating the long-lasting region of highly circular flow, and the bending of the vortex towards the leading edge near the blade mid-span. After some delay, a second spanwise vortex seems to form as well (Fig. 13(c)). Due to the superposition of the axial flow, velocities seen by the rotor blade and consequently angles of attack change non-linearly along the span. Furthermore, the axial free stream velocity adds – as a vector – to the resultant flow velocity seen by the blade and thus slightly increases the blade Mach number, which is known to lower the angle of attack at which dynamic stall occurs[16]. Overall changes in flow field and evolution of vortical structures are supposed to correlate with the lower maximum integral loads reached in case three.

## 5. CONCLUSIONS

Numerical investigations of three-dimensional dynamic stall on a two-bladed rotor with 1/rev cyclic pitch control were conducted with DLR's block-structured finite-volume RANS solver FLOWer. The Menter SST




(a) $\psi = 218.0°$, $\theta_{75} = 23.3°$ ↑

(b) $\psi = 224.0°$, $\theta_{75} = 24.0°$ ↑

(c) $\psi = 234.0°$, $\theta_{75} = 25.2°$ ↑

**Fig. 13.** Visualization of dynamic stall on a pitching rotor blade with $\theta_{75} = 17.2° - 10° \sin(\psi)$ and a superimposed axial flow (case three). Left: Instantaneous isosurfaces of the $\lambda_2$-criterion colored with $p/p_\infty$ and streamlines. Right: Instantaneous vorticity contours and in-plane streamlines at $r/R = 0.83$.

turbulence model was used along with a fifth-order spatial CRWENO scheme.

A grid and time-step dependency study was carried out and showed that both the setups with 22 million and 49 million grid cells and the time steps between 720 and 2000 steps per cycle captured key load characteristics of dynamic stall. However, slight differences were noticed regarding calculated maximum values and secondary dynamic stall events.

The main dynamic stall event occurred during the upstroke and in the outboard region of the rotor blade. Flow separation started near the leading edge around $r/R = 0.85$ and seemed to be shock-induced. While flow separation and lift generation moved inboard towards the mid-span quickly, outboard spreading appeared to be limited due to the interaction with the blade tip vortex. At $r/R \approx 0.9$ vortical structures appeared normal to the blade surface, inducing a long-lasting circular flow pattern with low surface pressure. A small range of outboard radial sections could be found, at which vortical structures and flow pattern resemble two-dimensional dynamic stall. The flow condition in this region seems to highly influence the point of lift and moment stall.

In the first two cases, a $\Omega$-shaped vortex and shortly after a partially spanwise vortex formed and convected downstream. During deep dynamic stall of

case two the blade tip vortex became distorted and finally collapsed, while a strong secondary dynamic stall event occurred. In case three, with a superimposed axial flow, the dynamic stall event was weakened and only one asymmetric arch-like vortical structure exhibited during primary dynamic stall. After stall, in all cases radial flow started to dominate, the overall flow pattern became highly three-dimensional and strong hysteresis effects became apparent.

For future numerical investigations and validations with experimental data, the usage of a Reynolds stress turbulence model (RSM) is planned to improve results in regions of strongly separated flow. Furthermore, a representation of vortices closer to reality is expected with a detached eddy simulation (DES) approach.

## REFERENCES


[1] McCroskey, W. J., *The Phenomenon of Dynamic Stall*, NASA TM 81264, 1981.

[2] Leishman, J. G., *Principles of Helicopter Aerodynamics*, Cambridge University Press, 2006.

[3] Klein, A., Lutz, T., Krämer, E., Richter, K., Gardner, A. D., and Altmikus, A., "Numerical Comparison of Dynamic Stall for Two-Dimensional Airfoils and an Airfoil Model in the DNWTWG," *AIAA Journal*, Vol. 57 (4), 2012, pp. 1–13.

[4] Gardner, A. D. and Richter, K., "Influence of Rotation on Dynamic Stall," *Journal of the American Helicopter Society*, Vol. 58 (3), 2013, pp. 1–9.

[5] Spentzos, A., Barakos, G., Badcock, K., Richards, B., Wernert, P., Schreck, S., and Raffel, M., "Investigation of Three-Dimensional Dynamic Stall Using Computational Fluid Dynamics," *AIAA Journal*, Vol. 43 (5), 2005, pp. 1023–1033.

[6] Kaufmann, K., Costes, M., Richez, F., Gardner, A. D., and Le Pape, A., "Numerical investigation of three-dimensional dynamic stall on an oscillating finite wing," 70th Annual Forum of the American Helicopter Society, Montreal, 2014.

[7] Nilifard, R., Zanotti, A., Gibertini, G., Guardone, A., and Quaranta, G., "Numerical Investigation of Three-Dimensional Effects on Deep Dynamic Stall Experiments," 71th Annual Forum of the American Helicopter Society, Virginia Beach, 2015.

[8] Schwermer, T., Richter, K., and Raffel, M., *Development of a Rotor Test Facility for the Investigation of Dynamic Stall*, DGLR-Fach-Symposium, STAB, 2014.

[9] Raddatz, J. and Fassbender, J. K., "Block Structured Navier-Stokes Solver FLOWer," *Notes on Numerical Fluid Mechanics and Multidisciplinary Design*, Vol. 89, 2005.

[10] Menter, F., "Two-Equation Eddy-Viscosity Turbulence Models for Engineering Applications," *AIAA Journal*, Vol. 32 (8), 1994, pp. 1598–1605.

[11] Richter, K., Le Pape, A., Knopp, T., Costes, M., Gleize, V., and Gardner, A. D., "Improved Two-Dimensional Dynamic Stall Prediction with Structured and Hybrid Numerical Methods," *Journal of the American Helicopter Society*, Vol. 56 (4), 2011, pp. 42001–42012.

[12] Ghosh, D., *Compact-Reconstruction Weighted Essentially Non-Oscillatory Schemes for Hyperbolic Conservation Laws*, Ph.D. thesis, University of Maryland, College Park, Md.,, 2013.

[13] Stanger, C., Kutz, B., Kowarsch, U., Busch, R., Keßler, M., and Krämer, E., *Enhancement and Applications of a Structural URANS Solver*, High Performance Computing in Science and Engineering, Stuttgart, 2014, pp. 435–446.

[14] Kowarsch, U., Keßler, M., and Krämer, E., "CFD-Simulation of the Rotor Head Influence to the Rotor-Fuselage Interaction," 40th European Rotorcraft Forum, Southampton, 2014.

[15] DiOttavio, J., Watson, K., Cormey, J., Komerath, N., and Kondor, S., "Discrete Structures in the Radial Flow Over a Rotor Blade in Dynamic Stall," 26th AIAA Applied Aerodynamics Conference, Honolulu, 2008.

[16] Chandrasekhara, M. S. and Carr, L. W., "Compressibility Effects on Dynamic Stall of Oscillating Airfoils," *AGARD CP-552*, 1994, pp. 3/1–3/15.

[17] Wolf, C. C., Merz, C. B., Richter, K., and Raffel, M., "Tip Vortex Dynamics of a Pitching Rotor Blade Tip Model," 53rd AIAA Aerospace Sciences Meeting, Kissimmee, 2015.